Multi-scale rupture growth with alternating directions in a complex fault network during the 2023 south-eastern Türkiye and Syria earthquake doublet

Ryo Okuwaki[1], Yuji Yagi[1], Tuncay Taymaz[2], Stephen P. Hicks[3]

[1]Faculty of Life and Environmental Sciences, University of Tsukuba, Tsukuba, Ibaraki 305-8572, Japan

[2]Department of Geophysical Engineering, The Faculty of Mines, Istanbul Technical University, Maslak, 34469 Sariyer, Istanbul, Türkiye

[3]Department of Earth Sciences, University College London, Gower Street, London, WC1E 6BT, UK

Key Points:

- An earthquake doublet of M_{W} 7.9 and M_{W} 7.6 ruptured multiple segments and curved faults
- A back-propagating supershear rupture of M_{W} 7.9 earthquake is triggered by the initial splay fault rupture
- Multi-scale rupture growth in a complex fault network may facilitate diverse rupture behaviors and triggering interactions in the doublet

Abstract

A devastating doublet of earthquakes with moment magnitude M_{W} 7.9 and M_{W} 7.6 earthquakes contiguously occurred in south-eastern Türkiye near the north-western border of Syria. Here we perform a potency-density tensor inversion to simultaneously estimate rupture evolution and fault geometry for the doublet. We find the initial M_{W} 7.9 earthquake involves a supershear back-rupture propagation, which is triggered by the initial bifurcated-fault rupture along a splay of the East Anatolian Fault and triggers the rupture in the southwest. The second M_{W} 7.6 event is triggered by the adjacent M_{W} 7.9 event, and it also involves supershear rupture along the favorably curved fault, which however is immediately stopped by geometric barriers in the fault ends. Our results highlight the multi-scale cascading rupture growth across the complex fault network that affects the diverse rupture geometries of the 2023 Türkiye earthquake doublet, contributing to the strong ground shaking and associated devastation.

Plain Language Summary

On 6 February 2023, devastating dual earthquakes; moment magnitude 7.9 and 7.6 events struck southern Türkiye near the northern border of Syria. The two earthquakes contiguously occurred, only separated in ~90 km and ~9 hours apart. The strong shaking

Corresponding author: Ryo Okuwaki, rokuwaki@geol.tsukuba.ac.jp

from the two earthquakes caused significant damage to the buildings and people, having caused over 50,000 fatalities in Türkiye and Syria. The source region is where the Anatolian, Arabian and African plates meet, developing the network of faults that host the large devastating earthquakes. Seismological analyses using observed seismic waveforms are effective for rapidly estimating how the rupture of the two earthquakes evolves over such distinctively oriented and possibly segmented faults. We use the globally observed seismic records to simultaneously estimate rupture evolution and fault geometry of the earthquake doublet. We find the sequence of both earthquakes involves curved and segmented fault ruptures, including the back-propagating rupture for the initial earthquake, which is facilitated by the complex active fault network. The 2023 earthquake doublet displays the irregular rupture evolution and diverse triggering behaviors both in a single event and across the earthquake sequence, which provide critical inputs in both our understanding of earthquake-rupture dynamics and better assessment of future damaging earthquakes.

1 Introduction

The Eastern Mediterranean region is one of Earth's most active tectonic environments, where the Anatolian plate is extruded westward, escaping from the collision between the Arabian and Eurasian plates (McKenzie, 1972; Taymaz, Jackson, & McKenzie, 1991; Taymaz, Eyidogan, & Jackson, 1991; Taymaz et al., 2004). To the southeast of the Anatolian plate, the left-lateral East Anatolian Fault (EAF), along with the right-lateral North Anatolian Fault (NAF), accommodates the extrusion of the Anatolian plate (Jackson & McKenzie, 1984; Taymaz, Eyidogan, & Jackson, 1991; Taymaz et al., 2021). The EAF forms an intra-continental transform fault, which separates the Anatolian and Arabian plates (Fig. 1). Although the EAF has been less seismically active than that around the NAF since instrumental-based catalogues started (e.g., Ambraseys, 1989), the EAF has hosted magnitude M 7+ earthquakes in the past, for example, an M 7.1 1893 in Çelikhan, M 7.4 1513 in Pazarcık, and an M 7.5 in 1822 to the east of Hassa (Ambraseys, 1989; Ambraseys & Jackson, 1998; Duman & Emre, 2013). Most recently, in 2020, a moment magnitude M_{W} 6.8 Doğanyol–Sivrice earthquake broke the region east of the 1893 M 7.1 earthquake (Melgar et al., 2020; Pousse-Beltran et al., 2020; Ragon et al., 2021; Taymaz et al., 2021), located to the north-east of the 2023 earthquakes focused in this study. The EAF is recognized to have multiple geometrically segmented faults and a series of bends, step-overs, and sub-parallel faults, leading to complex fault networks (Fig. 1) (e.g., Duman & Emre, 2013). This complexity is particularly evident in southern Türkiye, where the EAF connects to the triple junction of the Anatolian, Arabian and African plates, and the main plate boundary merges into the Dead Sea Fault (DSF) zone to the south. This diffuse zone of deformation manifests as a rotation in the strike of the main EAF from NE-SW in the NE to SSW-NNE in the town of Pazarcık, SW Kahramanmaraş province (Fig. 1). To the north of Kahramanmaraş province, the EW-oriented, the Sürgü fault zone (SFZ), obliquely branches from the main EAF (Arpat & Saroglu, 1972; Taymaz, Eyidogan, & Jackson, 1991; Duman & Emre, 2013; Duman et al., 2020). During a large earthquake, the orientation and speed of slip in such a complex network of faults contributes to ground shaking (e.g., Dunham & Bhat, 2008; Tsai & Hirth, 2020).

Two devastating earthquakes with M 7.7 and M 7.6 occurred on February 6, 2023 near the SW end of the EAF in Nurdağı-Pazarcık segment, SE Türkiye near the northern border of Syria (AFAD, 2023). The two earthquakes occurred only ∼9 hours and ∼90 km apart (Fig. 1). The epicenters reported by AFAD (2023) show that the initial M 7.7 earthquake seems to have initiated off the main EAF strand in the Narlıdağ fault zone (Duman & Emre, 2013), lying ∼15 km to the east (Fig. 1). In contrast, the secondary M 7.6 earthquake appears to be near the SFZ (Fig. 1). The relocated aftershocks (Melgar et al., 2023) seemingly align with the main EAF strand and the northern strand of the EAF, whilst some other linear trends and clusters can be seen off the main EAF segment; for example around the epicenter of the initial M 7.7 earthquake, the aftershocks elongate and intersect the main EAF (Fig. 1). The Global Centroid Moment Tensor (GCMT) solutions (Dziewonski et al., 1981; Ekström et al., 2012) for the two earthquakes have oblique left-lateral strike-slip faulting. The fault orientations of the two solutions are apparently consistent with the bulk orientations of the main EAF segment and the SFZ respectively (Fig. 1), however, the GCMT solutions show moderately high non-double couple components of 42% and 57%.

The geometric complexity of the EAF and the adjacent fault networks, apparent offset of the initial M 7.7 epicenter from the main EAF strand, high non-double couple components of the GCMT solutions, and the aftershock distribution with diverse orientations collectively suggest the earthquake sequence may have involved complexity of both the rupture evolution and fault geometry (Abercrombie et al., 2003; Okuwaki et al., 2021; Okuwaki & Fan, 2022). In general, geometric complexities of a fault system are known to control rupture speed and direction, and triggering of separated fault segments (Das & Aki, 1977; Kase & Day, 2006; Yıkılmaz et al., 2015; Huang, 2018). There is also growing observational evidence of rupture irregularity in the complex fault damage zones in different tectonic regimes, such as transient supershear ruptures across fault bends (Bao et al., 2019; Socquet et al., 2019), triggering of ruptures with different faulting styles and on different segments (Nissen et al., 2016; Fan & Shearer, 2016; Okuwaki & Fan, 2022), and apparent rupture back-propagation or re-rupture (Hicks et al., 2020; Vallée et al., 2023; Yamashita, Yagi, & Okuwaki, 2022; Yagi et al., 2023). Such diverse rupture behavior among such complex tectonic environments and fault zones gives fundamental inputs that deepen and accelerate our understanding of earthquake-source physics and the knock-on effects on strong ground motion. However, it has been challenging for seismologists to rigorously retrieve rupture complexity that should be recorded in rich waveform datasets, because of the necessity of assumptions involving the fault geometry and rupture direction, which are often not necessarily required by the data itself and sometimes bias the interpretation of the earthquake source process. The methodological difficulties in analyzing geometrically complex earthquakes are a huge obstacle in our understanding of earthquake source physics, but also hinder rapid and robust response, especially for destructive events like the 2023 SE Türkiye and Syria earthquake sequence, and assessing of future earthquake (e.g., aftershock) hazard in the short-to-medium term.

Here we report a narrative of rupture evolution of the two M 7.7 and M 7.6 earthquakes using teleseismic P-waveforms observed globally at broadband seismic stations. We find the two nearby earthquakes ruptured multiple segments and branches of the

EAF, and involving curved faults, which likely influence slip acceleration and deceleration during discrete rupture episodes. Most notably, the initial M 7.7 earthquake involves an apparent back-propagating supershear rupture through and beyond the hypocenter area, which should be responsible for the series of triggering of sub-events in their unfortunately favorable orientation.

2 Materials and Methods

In general, finite fault inversion estimates the spatio-temporal slip distribution on an assumed fault plane (Olson & Apsel, 1982; Hartzell & Heaton, 1983). Such modeled fault geometries may be refined using field observations and satellite imagery that captures the surface deformation. However, strictly prescribing fault geometry may bias our interpretation of the solution, because limiting model flexibility can mask hidden rupture details and fault geometries beyond can sometimes be observed at the surface (e.g., Shimizu et al., 2020). Similar problems may arise when strict assumptions are made about kinematic information such as rupture velocity and direction.

In this study, we perform a recently developed potency-density tensor inversion (Shimizu et al., 2020; Yamashita, Yagi, Okuwaki, Shimizu, et al., 2022) for both the M 7.7 and M 7.6 earthquakes using teleseismic P-waves. Our approach is particularly effective for analyzing complex earthquake sequences, because it does not require any detailed assumptions about the fault geometry, but rather, we solve for the fault geometry as data requires. In this study, we configure the model-space geometry based on the recognized active faults (Emre et al., 2018) and the relocated aftershocks (Melgar et al., 2023) around the source region of the two earthquakes (Fig. S3). Regardless of this model-space parameterization, one strength of our approach the potency tensors at each source element are still flexible to represent fault geometry that deviates from the prescribed model-fault geometry. This modeling flexibility of our approach is particularly advantageous for analyzing an earthquake in a complex fault zone, where there are multiple segments of faults with different orientations, and possible supershear ruptures, which are likely factors for the 2023 SE Türkiye earthquake doublet given the strike-slip configuration and known structure of the EAF.

We adopt a maximum rupture-front speed of 4 km/s so that we may be able to capture possible supershear rupture or inter-subevents dynamic triggering within the model space based on the local seismic velocities around the source region (Table S1). We also adopt a sufficiently long maximum slip duration at each source element of 42 s and a total source duration of 80 s for the initial earthquake and a maximum slip duration at each source element of 20 s and a total source duration of 20 s for the second earthquake (Fig. 2). These values are chosen so that each source element can represent multiple slip episodes, especially in the case of rupture back-propagation or re-rupture.

Our approach bridges the gap between conventional finite fault inversions, discrete sub-event parameterisations, and seismic back-projection, the latter requiring very few assumptions about the fault geometry and rupture information (Ishii et al., 2005; Y. Xu et al., 2009; Meng et al., 2012; Nissen et al., 2016; Satriano et al., 2012; Yao et al., 2011; Taymaz et al., 2021). Still, our approach additionally provides kinematic information by directly solving for the potency-rate density distribution. To perform a stable inversion with such a high degree-of-freedom model without overfitting, the uncertainty of the Green's function is incorporated into the data covariance matrix (Yagi & Fukahata, 2011) and the strength of smoothing is adjusted using the Akaike's Bayesian Information Criterion (e.g., Akaike, 1980; Yabuki & Matsu'ura, 1992; Sato et al., 2022).

We apply a standardized data processing workflow for our potency-density tensor approach that has been applied to earthquakes in different tectonic regimes (Shimizu et al., 2020; Tadapansawut et al., 2021; Hu et al., 2021; Fan et al., 2022; Fang et al., 2022; Hicks et al., 2020; Yamashita, Yagi, Okuwaki, Shimizu, et al., 2022; Yagi et al., 2023). We use the vertical component of teleseismic P-waveforms from a total of 39 and 37 stations for the M 7.7 and M 7.6 earthquakes, respectively (Figs. S1 and S2). The data are selected to ensure the azimuthal coverage of the stations so that we can resolve potential variations of radiation pattern during the rupture evolution and hence the spatiotemporal change of fault geometry. We also select data with the highest signal-to-noise ratio so that we manually pick the first motion of P-wave (Okuwaki et al., 2016) that accounts for 3-D heterogeneity of Earth's structure (Fan & Shearer, 2015). The data are then restituted to velocity at 1.0-s sampling interval by removing the instrumental responses. Green's functions are calculated based on the method of Kikuchi and Kanamori (1991), adopting CRUST1.0 model (Laske et al., 2013) for the one-dimensional layered velocity structure around the source region (Table S1). The initial rupture point is adopted from the relocated epicenter for the M 7.7 earthquake (Melgar et al., 2023) and on the model fault near the relocated epicenter for the M 7.6 earthquake, and the hypocentral depth is set at 15-km depth for both earthquakes (Fig. S3). The uniformly-distributed model source elements are spaced 10×5 km and 5×5 km in the along-strike and dip directions for the M 7.7 and M 7.6 earthquakes, respectively, which are regularly distributed along the vertically dipping non-planar model fault that aligns with the active faults (Emre et al., 2018) and the relocated aftershocks (Fig. S3). Together with the curved main EAF strand, we adopt a splay fault into our model fault centered on the initial rupture point, which is orienting at 35° NE, having an acute angle relative to the main EAF in NE direction (Fig. S3).

3 Results

3.1 Initial M_W 7.9 Nurdağı-Pazarcık earthquake

Our potency-density tensor inversion finds the first earthquake ruptured a total of 350 km length, 200 km length northeast from the epicenter and 150 km southwest of the epicenter along our modeled fault, including the splay fault domain (Figs. 2 and S4). The total seismic moment is 9.6×10^{20} N m (M_W 7.9). The overall faulting mechanism indicated by the flexible potency density tensors is consistent with our prescribed non-planar model fault geometry (Fig. 2). The potency-density tensors show a largely planar fault with depth. The space-time evolution of the rupture shows four distinct episodes which we describe in the following paragraphs.

Rupture Episode 1. The rupture first initiates at the hypocentre, and then propagates bilaterally toward the NE and SW for the first 10 s after origin time (OT), extending 25 km either side of the hypocenter along the splay fault. The moment-rate release of this initial rupture episode is minor, having only 3% of the total seismic moment (M_W 6.9).

Our potency-rate density tensor solution shows the fault orientation corresponding to the left-lateral faulting with a median strike of 37° (e.g., 7–8 s time window; Fig. 3), consistent with the prescribed splay fault and less consistent with the main EAF (Fig. 3). The first-motion faulting mechanism using local-regional waveforms (Fig. 3) indicates this rupture initiated along a fault plane with a similar strike, but with an oblique-normal sense of slip.

Rupture Episode 2. After a relative quiescence for 5 s after the end of the first episode, the second rupture episode starts at OT+15 s, lying 60 km NE of the epicenter. This second rupture episode releases the greatest amount of seismic moment (35%; M_W 7.6) of the entire rupture. The rupture propagates in an asymmetric bilateral manner with a strong SW-oriented direction, rupturing a total length of 120 km over 20 s duration. Most notably, the SW flank of the rupture front apparently back-propagates through the hypocentral region beyond 20 km SW of the epicenter (Fig. 2). Even after accounting for smoothing constraints applied to our inversion, the migration speed of the associated SW-directing back-propagating rupture signal is in a range of ∼5–6 km/s that exceeds the local S-wave velocity (Table S1; Laske et al., 2013) (Fig. 2; Movies S1 and S2), indicating a super-shear rupture. Although the rigorous estimates of rupture velocity can be limited due to the smoothing constraints, the migration speed of this high slip-rate zone is related to the rupture-front velocity (Okuwaki et al., 2020). The fault geometry estimated from our potency-density tensor approach shows vertical strike-slip faulting with a median strike of 55° (e.g., 22–23 s; Fig. 3) that is much more consistent with the main EAF.

Rupture Episode 3. A third rupture phase NE of the hypocentre begins to be dominant from OT+35 s, soon after the SW back-rupture propagation decays. It first propagates to the SW near the NE flank of the second rupture episode at the migration speed of 5–6 km/s, but then the NE-oriented component of the bilateral rupture becomes more dominant during OT+37–45 s with an apparently fast migration, rupturing a total length of 100 km until it immediately stops near the NE edge of the model domain at 120 km NE from the epicenter (Fig. 2) with 15% of the total seismic moment (M_W 7.4). The strike orientation is similar to that of the SW back-rupture and remains consistent with the main EAF.

Rupture Episode 4. A fourth rupture episode starts at OT+45 s in the SW corner of the model domain, partially overlapping in space with the second rupture. The rupture front unilaterally propagates toward the SW at fast, supershear speed, exceeding the local S-wave velocity during OT+45–55 s with the apparent migration speed of 6–7 km/s. Then, the rupture front apparently slows down at ∼150 km SW from our junction of the EAF and splay model faults, and stops at 75 s. The median strike orientation shows 54° (e.g., 50–51 s time window). The fourth rupture episode has 43% of the total seismic moment (M_W 7.7), and the potency-density tensors display the median non-double couple component of 24% (e.g., 60–61 s; Fig. 3).

3.2 Secondary M_W 7.6 Ekinözü earthquake

The rupture process of the later M 7.6 has a more confined nature, which ruptures 80 km length and 20 km width over a single episode, and the total seismic moment is 3.2×10^{20} N m (M_W 7.6). The rupture evolution is asymmetric bilateral with a dominant westwards-directed rupture from the epicenter. The west-oriented rupture propagates at a fast migration speed of 5–6 km/s from 6 to 10 s, which again exceeds the local S-wave velocity (Table S1; Fig. 2; Movies S1 and S2). The rupture immediately stops at around 15 s. The fault geometry estimated from our potency-density tensors has an EW-oriented curved fault strike with strike-slip faulting, which is well aligned with the prescribed curved model plane geometry. The estimated fault dip is dominantly vertical, but the dip angle slightly shallows with depth from 76° to 61°, as defined by the maximum along-strike potency density (Fig. S4b). Near the end of the rupture, dip-slip faulting components become dominant at the tips of the main rupture, with strikes rotated north-south (Fig. 3).

4 Discussion

4.1 M_W 7.9 event: rupture initiation on a splay fault to the main EAF

The initial rupture of the M_W 7.9 event has a different fault orientation than that of the following main bilateral rupture that releases most (97%) of the seismic moment. For example, during the peak slip of the first rupture episode (7–8 s), the median strike is 37°, whilst the later bilateral rupture episode has a median strike of 55° (Fig. 3). In the initial rupture domain, intense aftershock activity is observed NE of the epicenter (Melgar et al., 2023), in a lineation oriented SW to NE, seemingly connecting to the main EAF strand at ∼35°. The alignment of these aftershocks on the splay fault is consistent with the strike orientation estimated from our inversion. To the east of the epicenter, the Narlıdağ fault zone has been mapped to extend to the N and NE (Perinçek & Çemen, 1990; Duman & Emre, 2013). From the rapid analyses of the satellite images and field measurements, surface rupture is also observed near the epicenter, which is elongated NE and is consistent with our estimated strike orientation (Reitman et al., 2023), which is called as Nurdağı-Pazarcık fault by Melgar et al. (2023). Given the hypocenter location, first motion mechanism, aftershock lineation, and the mapped active faults and surface ruptures near the epicenter, it is likely that the first rupture episode occurred on a sub-parallel splay fault to the main EAF and initiated with an oblique-normal faulting mechanism. The relative angle of our estimated strike orientations between the splay fault and the main EAF model domain is ∼18°, which is close to the peak of the splay angle distributions (±17°) observed in the active fault system in California (Ando et al., 2009; Scholz et al., 2010). In between the first and second rupture episodes, we only see the minor moment release, and these two episodes are not apparently physically connected to each other.

4.2 Rupture dynamics during apparent back-propagating slip

One of the notable features of the M_W 7.9 earthquake is the main asymmetric bilateral rupture of the second episode during OT+15–35 s (Fig. 2), where the SW flank of the bilateral rupture apparently propagates back through the hypocentral area. Such a boomerang-like back rupture propagation is an end-member rupture behavior that has become more frequently reported with higher-resolution datasets and more detailed rupture imaging (Meng et al., 2018; Hicks et al., 2020; Yamashita, Yagi, & Okuwaki, 2022; Vallée et al., 2023). However, in all of these cases, data were not ground-truth fine-scale rupture details that could explain the apparent back-rupture propagation because the earthquakes studied were either deep or in remote areas. Therefore, the apparent boomerang rupture of the 2023 SE Türkiye earthquake is intriguing because we show that the rupture propagated along different sub-parallel fault strands which could help to explain these previously reported examples of back-propagating ruptures.

Although it is still difficult to find a deterministic explanation of why the initial rupture occurred not on the main EAF, but on the bifurcated minor fault, the series of multiple ruptures that are responsible for the resultant boomerang-like rupture can be explained by a cascading up of rupture size based on a hierarchical rupture model (e.g., Ide & Aochi, 2005; Otsuki & Dilov, 2005). In this case, with the initial rupture on the shorter, bifurcated minor splay and the secondary, longer rupture, the secondary rupture can be dynamically triggered by the initial rupture propagation as it cascades up to the longer scale of the rupture. The main EAF should have accumulated enough strain due to the plate accommodation (e.g., Aktug et al., 2016; Weiss et al., 2020), which makes it ready to be ruptured once assisted by the initial rupture on the bifurcated fault.

Rupture dynamics across branching faults have been extensively studied by the numerical simulations (Kame et al., 2003; Ando & Yamashita, 2007; Aochi et al., 2000; Bhat et al., 2007; S. Xu et al., 2015; Okubo et al., 2020). Backward branching rupture is particularly proposed (Fliss et al., 2005), where the stress accumulation at the tip of the main fault enhances rupture jump onto the neighboring branch fault, which nucleates bilateral rupture, where of which one flank can be seen as apparent backward rupture. Although it remains to be solved whether the initial rupture is physically intersecting the main EAF or not, our source model shows that the initial rupture is not continuously propagating with a resolvable slip-rate into the main EAF, and the second rupture episode begins on the main EAF $\sim$20 km SW from the apparent junction of the initial fault strand and the main EAF. The spatiotemporal gap between the initial and second rupture episodes might play a role to enable the cascade up or jump of rupture to the larger scale main rupture. The main EAF west of the junction with the Narlıdağ fault zone should be situated in the extensional quadrant of the left-lateral Rupture Episode 1, which may impart a stress shadow on the main EAF. Such a stress shadow may have disrupted the SW-directed Rupture Episode 2, which we see as a temporary rupture deceleration at OT+15–20 s before it then accelerated to supershear (Fig. 2). The rupture propagation toward SW through the hypocentral region may be enabled because the longer-scale main EAF rupture should have enough fracture energy to easily overcome the area affected by the stress shadow possibly generated by the lower level of rupture episode.

The strike orientation during the second rupture episode (OT+15–20 s) is slightly rotated clockwise, which is also mapped in the main EAF strand west of the junction (Figs. 1 and 3). If this change in fault orientation acts as a restraining bend given the background stress field, the rupture propagation may cause a concentration of stress at the bend. This might have caused the rupture deceleration, which can be seen as the slip stagnation during OT+15–20 s. Soon after this pause, dynamic stresses allowed the rupture to continue and propagate to the SW and even accelerate its speed, which can be consistent with the predicted behavior of the supershear rupture transition across restraining bends (e.g., Bruhat et al., 2016).

We further note that the NE and SW boundaries of the second rupture episode coincide with the fault steps near Gölbaşı and south of Nurdağı regions seen from the active faults (see locations S1 and S2 in Fig .S5). The apparent delay times between the second rupture episode and the following episodes are also worth noting, which takes 10 s between the NE-end of the second rupture to the third rupture nucleation (location S1; OT+25–35 s) and also 10 s between the SW-end of the second rupture and the fourth rupture (location S2; OT+35–45 s) (Fig. S5). We do not have enough evidence to explain how such episode gaps are physically connected, but it will stimulate further research to investigate how the rupture evolved across fault steps with such delay times, for example, the long nucleation processes or possibly inter-subevent slow deformation.

4.3 The SW-end third rupture episode broke multiple fault segments

Together with the radiation pattern of the left-lateral faulting, the strong directivity of the SW-oriented back rupture process can result in a further cascading of the rupture toward the SW. Our source exhibits a relatively fast and smooth rupture along the section near Nurdağı, whilst it suddenly slows down at 55 s, where the rupture intersects at the apparent left-step seen in the active fault strand south of Hassa (Fig. 1).

The strike orientation extracted from the best-double-couple solution of our estimated potency-density tensors is not apparently aligned with the bulk linear trend of the active faults (Fig. 2). However, because we observe non-double-couple fractions for the SW end rupture (e.g., 24% during 60–61 s; Fig. 3), it should still be too early to define which individual fault strands likely ruptured. South of Hassa, several distinct fault segments are separated by step-overs (Fig. 3) (Duman & Emre, 2013). The aftershock distribution here also displays a more scattered nature than the other section along the main EAF and the one near the epicenter; however, we cannot rule out a greater earthquake location uncertainty due to diminished regional seismic network coverage close to the Syria border. Pre-earthquake field measurements (Emre et al., 2018; Duman & Emre, 2013), as well as the fault rupture mapping immediately after the 2023 earthquakes (Reitman et al., 2023) shows a zigzag geometry involving the bends and curves. This evidence collectively suggests that the later phase of rupture may have involved multiple faults with different geometries in the SW.

4.4 M_{W} 7.6 event: curved and focused rupture

We find the M_{W} 7.6 earthquake shows a much more focused rupture process, compared with the preceding M_{W} 7.9 event. Yet, our solution finds that the strike of the ruptured fault geometry curves gradually, with a counterclockwise rotation toward the west. The rotation trend can favorably be oriented to the optimal plane of the background horizontal stress given the bulk E-W oriented left-lateral strike-slip system of the Sürgü fault zone. This trend can thus help to rupture propagation, in a similar way to a fault-releasing bend (e.g., Kase & Day, 2006). In addition, such a favorably curved fault geometry may have facilitated the supershear rupture (e.g., Trugman & Dunham, 2014; Bruhat et al., 2016), albeit over a relatively short distance. At the western and eastern ends of the model domain, we find a significant change of mapped fault geometry and the orientation of the potency density tensors. At these domains, the strike orientation is almost NS, and dip-slip becomes dominant. The complex network in Gŏksun-Savrun faults to the west and Nurhak Fault complex to the east (Duman & Emre, 2013) can explain such the significant change of fault geometry, asymmetric nature of the bilateral rupture, and the likely reason for abrupt rupture termination at both ends.

The collocation of the two M_W 7.9 and M_W 7.6 earthquakes, only separated around 9 hours apart, may give rise to a question over how the initial M_W 7.9 earthquake can affect and possibly trigger the later M_W 7.6 earthquake. Such earthquake doublets have been reported before in different tectonic environments (e.g., Lay & Kanamori, 1980; Astiz & Kanamori, 1984; Nissen et al., 2016; Ammon et al., 2008; Fan et al., 2016; Lay et al., 2013; ten Brink et al., 2020; Hicks & Rietbrock, 2015; Ross et al., 2019; Jiang et al., 2022; Yagi et al., 2023). Our Coulomb stress analyses using our estimated source model shows the M_W 7.9 earthquake may have induced positive static stress change in the hypothesized M_W 7.6 source domain (~0.4 bar) (Fig. S6), which may have brought the fault that hosted the M_W 7.6 earthquake closer to failure.

Conclusions

We find the differently oriented, curved, and multiple fault segments facilitate the series of complex rupture geometries during the devastating earthquakes in 2023. Back-propagating supershear rupture during the initial M_W 7.9 earthquake is facilitated by the branching fault rupture that provides an initial stress trigger to the larger-scale main EAF rupture. The secondary M_W 7.6 earthquake involves the westward supershear rupture, which is abruptly interrupted by the geometric barriers in both the western and eastern ends of the northern strand of the EAF, being responsible for the relatively focused source nature. Our results suggest the geometrically complex fault network around the source region should be key to developing multi-scale cascading rupture growth and alternating rupture directions, which will be critical inputs for both our understanding of earthquake source physics and better assessment of the future damaging earthquakes in complex fault zones.

Open Research

Materials presented in this paper are archived and available at https://doi.org/10.5281/zenodo.7678181. The seismic data were downloaded through the IRIS Wilber 3 system (https://ds.iris.edu/wilber3/find_event) or IRIS Web Services (https://service.iris.edu). We used ObsPy (https://doi.org/10.5281/zenodo.165135; Beyreuther et al., 2010), Pyrocko (https://pyrocko.org/; Heimann et al., 2017), matplotlib (https://doi.org/10.5281/zenodo.592536; Hunter, 2007), Cartopy (https://doi.org/10.5281/zenodo.1182735; Met Office, 2015; Elson et al., 2022), Generic Mapping Tools (https://doi.org/10.5281/zenodo.3407865; Wessel & Luis, 2017); and Scientific colour maps (https://doi.org/10.5281/zenodo.1243862; Crameri, 2018; Crameri et al., 2020) for data processing and visualization. First motion mechanisms were picked using waveform data from the following seismic networks: KO (https://doi.org/10.7914/SN/KO); IM (https://www.fdsn.org/networks/detail/IM/); TK (https://doi.org/10.7914/SN/TK); and TU (https://doi.org/10.7914/SN/TU).

Acknowledgments

We thank editors and reviewers for their evaluations of this manuscript. The facilities of IRIS Data Services, and specifically the IRIS Data Management Center, were used for access to waveforms, related metadata, and/or derived products used in this study. IRIS Data Services are funded through the Seismological Facilities for the Advancement of Geoscience (SAGE) Award of the National Science Foundation under Cooperative Support Agreement EAR-1851048. We appreciate the Disaster and Emergency Management Presidency of Türkiye (AFAD) for providing an initial catalogue of aftershocks and phase-arrival data acquired from their bulletin resources. This work was supported by JSPS Grant-in-Aid for Scientific Research (C) 19K04030 and 22K03751 and Early-Career Scientists 20K14570. The authors declare no conflicts of interest relevant to this study.

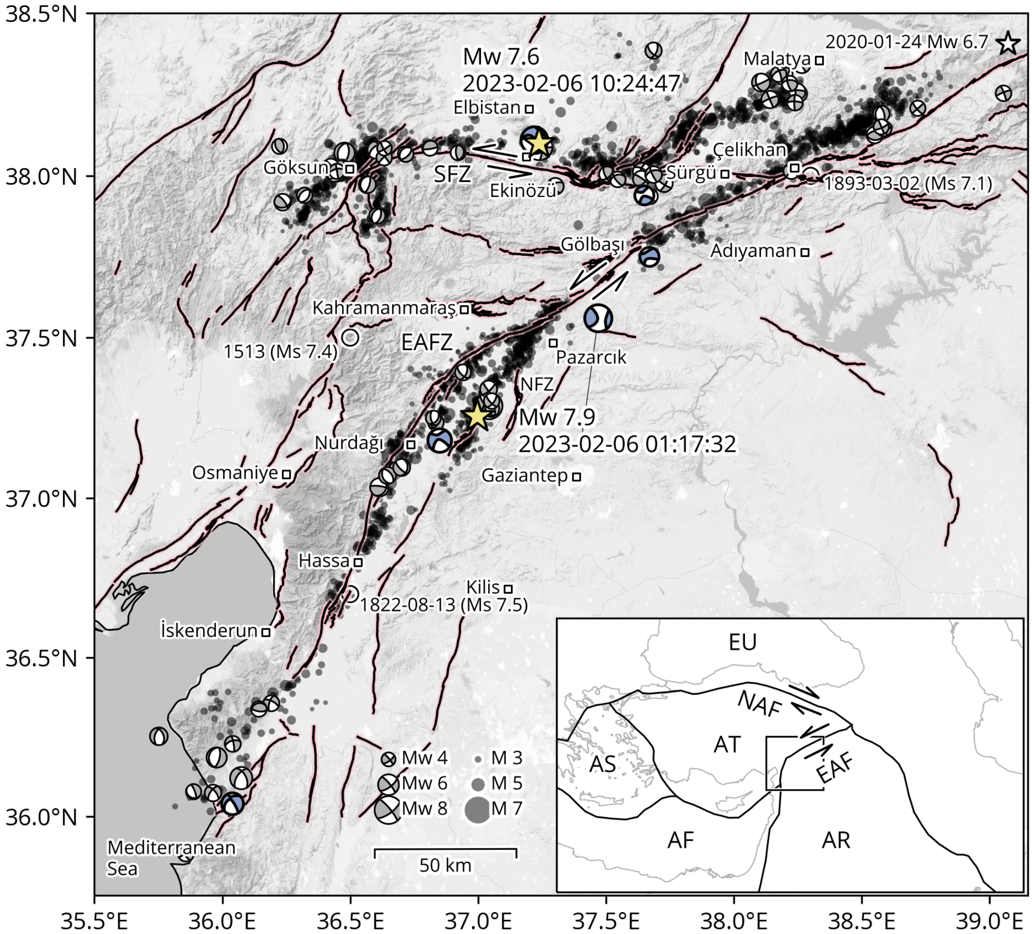

Figure 1. Summary of the study region. The yellow stars are the relocated epicenters of the M_W 7.9 and M_W 7.6 earthquakes. The dots are the relocated aftershocks ($M \geq 1.1$) from 2023-02-06 01:17:32 (UTC) to 2023-02-16 21:35:55 (UTC) (after Melgar et al., 2023). The blue beachballs are the GCMT solutions (Dziewonski et al., 1981; Ekström et al., 2012) and the gray beachballs are the focal mechanisms determined by the AFAD (AFAD Focal Mechanism Solution, 2023) during the 2023 earthquake sequence. The active faults are from Emre et al. (2018), including the East Anatolian Fault Zone (EAFZ), Sürgü Fault Zone (SFZ), and Narlıdağ fault zone (NFZ). The square markers locate major provinces and towns. The white star is the epicenter of the 2020 M_W 6.7 Doğanyol–Sivrice earthquake (Taymaz et al., 2021). The circles are the epicenters of the historical earthquakes (Ambraseys, 1989; Ambraseys & Jackson, 1998). The basemap tiles (terrain) including the administrative boundaries are provided by Stamen Design (under CC BY 3.0 license) and OpenStreetMap (under ODbL license). The inset map shows the boundaries between Aegean Sea (AS), African (AF), Anatolian (AT), Arabian (AR), and Eurasian (EU) plates (Bird, 2003). The arrows denote the relative motion of the EAF and the NAF. The square box outlines the map extent of Fig. 1.

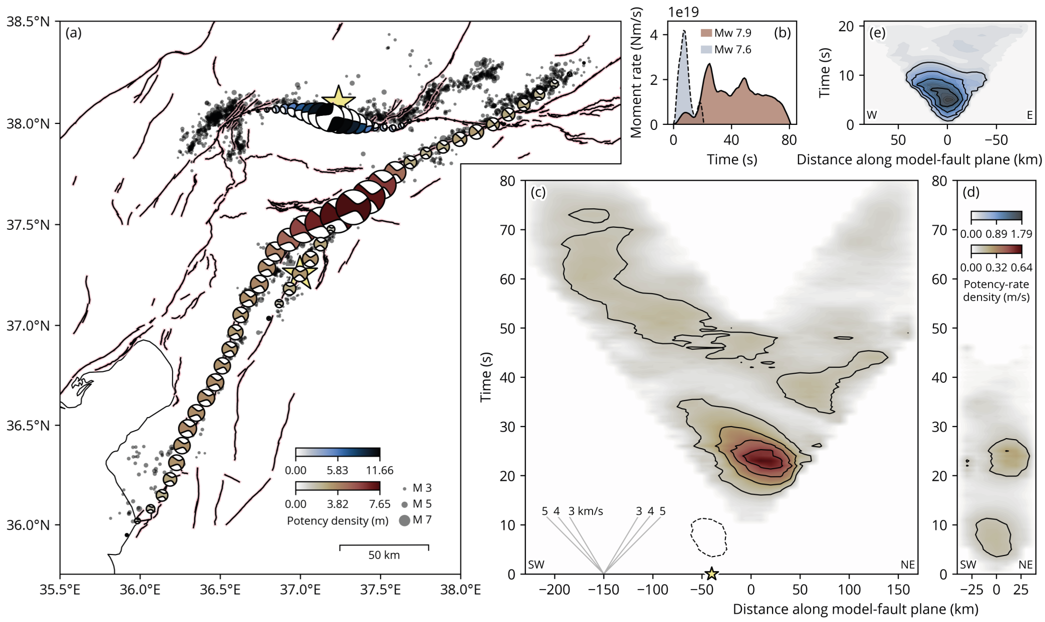

Figure 2. Summary of our solutions for the M_W 7.9 and M_W 7.6 earthquakes. (a) The beachball shows the lower-hemisphere projection of the moment tensor calculated by integrating the potency-rate density tensors with respect to time at each source element, with its size scaled with the potency density. Only the moment tensors with the maximum potency density along depth are shown. A full set of the potency-density tensors are shown in Fig. S4. The stars, dots, and lines are the same as shown in Fig. 1. (b) The moment-rate functions. The right panels show the spatiotemporal distributions of the potency-rate density for (c,d) the M_W 7.9 and (e) the M_W 7.6 earthquakes, projected along the non-planar model faults. The "0" on the X-axis of panel (c) corresponds to the location of junction between the splay fault and the main EAF, while "0" of panel (d) corresponds to the initial rupture point on the splay fault. The star shows the location of the source element on the EAF that is closest to the initial rupture point on the splay fault. The dashed contours show the potency-rate density on the splay fault during OT+0–15 s projected onto the approximate location on the main EAF model domain. The panel (d) is the splay fault domain for the M_W 7.9 earthquake. The abscissa shows the distance along the model fault. The dashed lines are the reference rupture speeds. The black contours are drawn at every 0.13 m/s (lower panels) and 0.36 m/s (upper panel) for the M_W 7.9 and the M_W 7.6 earthquakes, respectively. The panel (d) is flipped horizontally so that it can intuitively be compared with a map view of the corresponding model.

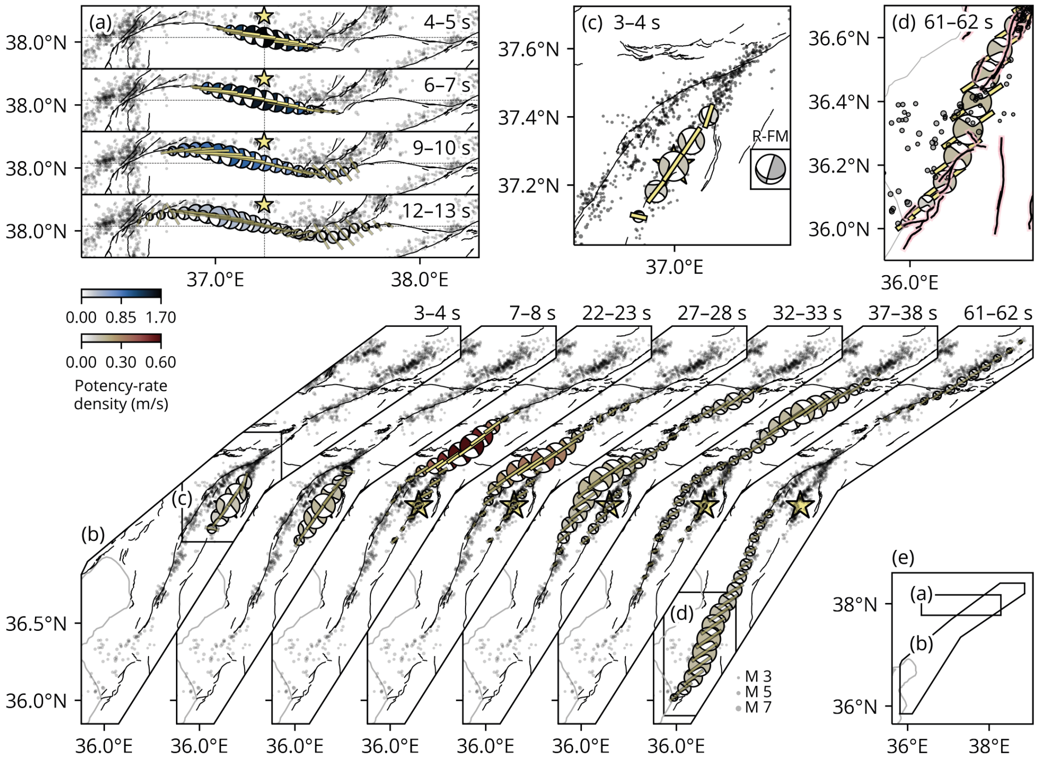

Figure 3. Selected snapshots of the spatiotemporal potency-rate density tensor distributions for (a) the M_W 7.6 and (b) M_W 7.9 earthquakes. The time window for the snapshot is shown on the corresponding panel. The yellow bar is the strike orientation extracted from the best-fitting double-couple components of the resultant potency-rate density tensors. The size of the beachball is scaled by the maximum potency-rate density in the corresponding time window. The optimum strike angle is one of the two possible nodal planes that minimizes the inner product of fault-normal vectors of the candidate plane and the reference fault plane: 54°/90° and 261°/90° (strike/dip) for the M_W 7.9 and the M_W 7.6 earthquakes, respectively. Only the source elements of the maximum potency-rate density along depth are shown. The full snapshots are shown in Movies S1 and S2. Panels (c) and (d) show the enlarged view of the initial and fourth rupture episodes, respectively. The inset on (c) shows the best-fitting focal mechanism: 197°/86°/56° (strike/dip/rake) determined by first-motions recorded by seismometer and strong-motion stations up to 350 km away (see Open Research) using the method of Hardebeck and Shearer (2002) with takeoff angles computed in the velocity model of Melgar et al. (2020). The stars, dots, and lines are the same as shown in Fig. 1. Panel (e) shows the map extents of (a) and (b).

References

Abercrombie, R. E., Antolik, M., & Ekström, G. (2003). The June 2000 M w 7.9 earthquakes south of Sumatra: Deformation in the India-Australia Plate . *J. Geophys. Res. Solid Earth*, *108*(B1), ESE 6–1–ESE 6–16. doi:10.1029/2001jb000674

AFAD. (2023). *AFAD (Disaster and Emergency Management Presidency) Earthquake Catalog.* Retrieved from https://deprem.afad.gov.tr/event-catalog

AFAD Focal Mechanism Solution. (2023). AFAD Focal Mechanism Solution. Retrieved from https://deprem.afad.gov.tr/event-focal-mechanism

Akaike, H. (1980). Likelihood and the Bayes procedure. *Trab. Estad. Y Investig. Oper.*, *31*(1), 143–166. Retrieved from https://doi.org/10.1007/BF02888350 doi:10.1007/BF02888350

Aktug, B., Ozener, H., Dogru, A., Sabuncu, A., Turgut, B., Halicioglu, K., ... Havazli, E. (2016). Slip rates and seismic potential on the East Anatolian Fault System using an improved GPS velocity field. *J. Geodyn.*, *94-95*, 1–12. Retrieved from http://dx.doi.org/10.1016/j.jog.2016.01.001https://linkinghub.elsevier.com/retrieve/pii/S0264370716300102 doi:10.1016/j.jog.2016.01.001

Ambraseys, N. N. (1989). Temporary seismic quiescence: SE Turkey. *Geophys. J. Int.*, *96*(2), 311–331. Retrieved from https://academic.oup.com/gji/article-lookup/doi/10.1111/j.1365-246X.1989.tb04453.x doi:10.1111/j.1365-246X.1989.tb04453.x

Ambraseys, N. N., & Jackson, J. A. (1998). Faulting associated with historical and recent earthquakes in the Eastern Mediterranean region. *Geophys. J. Int.*, *133*(2), 390–406. Retrieved from https://academic.oup.com/gji/article/133/2/390/578275 doi:10.1046/j.1365-246X.1998.00508.x

Ammon, C. J., Kanamori, H., & Lay, T. (2008). A great earthquake doublet and seismic stress transfer cycle in the central Kuril islands. *Nature*, *451*(7178), 561–565. Retrieved from http://www.nature.com/articles/nature06521 doi:10.1038/nature06521

Ando, R., Shaw, B. E., & Scholz, C. H. (2009). Quantifying Natural Fault Geometry: Statistics of Splay Fault Angles. *Bull. Seismol. Soc. Am.*, *99*(1), 389–395. Retrieved from https://pubs.geoscienceworld.org/bssa/article/99/1/389-395/350160 doi:10.1785/0120080942

Ando, R., & Yamashita, T. (2007). Effects of mesoscopic-scale fault structure on dynamic earthquake ruptures: Dynamic formation of geometrical complexity of earthquake faults. *J. Geophys. Res. Solid Earth*, *112*(9), 1–15. doi:10.1029/2006JB004612

Aochi, H., Fukuyama, E., & Matsu'ura, M. (2000). Selectivity of spontaneous rupture propagation on a branched fault. *Geophys. Res. Lett.*, *27*(22), 3635–3638. Retrieved from http://doi.wiley.com/10.1029/2000GL011560 doi:10.1029/2000GL011560

Arpat, E., & Saroglu, F. (1972). The East Anatolian fault system; thoughts on its development. *Miner. Res. Explor. Inst. Turkey*, *78*, 33–39. Retrieved from https://dergipark.org.tr/en/pub/bulletinofmre/issue/3904/52066

Astiz, L., & Kanamori, H. (1984). An earthquake doublet in Ometepec, Guerrero, Mexico. *Phys. Earth Planet. Inter.*, *34*(1-2), 24–45. Retrieved from https://

linkinghub.elsevier.com/retrieve/pii/0031920184900827 doi:10.1016/0031-9201(84)90082-7

Bao, H., Ampuero, J.-P., Meng, L., Fielding, E. J., Liang, C., Milliner, C. W. D., … Huang, H. (2019). Early and persistent supershear rupture of the 2018 magnitude 7.5 Palu earthquake. *Nat. Geosci.*, *12*(3), 200–205. Retrieved from http://dx.doi.org/10.1038/s41561-018-0297-zhttp://www.nature.com/articles/s41561-018-0297-z doi:10.1038/s41561-018-0297-z

Beyreuther, M., Barsch, R., Krischer, L., Megies, T., Behr, Y., & Wassermann, J. (2010). ObsPy: A Python Toolbox for Seismology. *Seismol. Res. Lett.*, *81*(3), 530–533. doi:10.1785/gssrl.81.3.530

Bhat, H. S., Olives, M., Dmowska, R., & Rice, J. R. (2007). Role of fault branches in earthquake rupture dynamics. *J. Geophys. Res.*, *112*(B11), B11309. Retrieved from http://doi.wiley.com/10.1029/2007JB005027 doi:10.1029/2007JB005027

Bird, P. (2003). An updated digital model of plate boundaries. *Geochemistry, Geophys. Geosystems*, *4*(3), 1105. doi:10.1029/2001GC000252

Bruhat, L., Fang, Z., & Dunham, E. M. (2016). Rupture complexity and the supershear transition on rough faults. *J. Geophys. Res. Solid Earth*, *121*(1), 210–224. doi:10.1002/2015JB012512

Crameri, F. (2018). Geodynamic diagnostics, scientific visualisation and StagLab 3.0. *Geosci. Model Dev.*, *11*(6), 2541–2562. doi:10.5194/gmd-11-2541-2018

Crameri, F., Shephard, G. E., & Heron, P. J. (2020). The misuse of colour in science communication. *Nat. Commun.*, *11*(1), 5444. doi:10.1038/s41467-020-19160-7

Das, S., & Aki, K. (1977). Fault plane with barriers: A versatile earthquake model. *J. Geophys. Res.*, *82*(36), 5658–5670. Retrieved from http://doi.wiley.com/10.1029/JB082i036p05658 doi:10.1029/JB082i036p05658

Duman, T. Y., Elmacı, H., Özalp, S., Kürçer, A., Kara, M., Özdemir, E., … Uygun Güldoğan, Ç. (2020). Paleoseismology of the western Sürgü–Misis fault system: East Anatolian Fault, Turkey. *Mediterr. Geosci. Rev.*, *2*(3), 411–437. Retrieved from https://doi.org/10.1007/s42990-020-00041-6http://link.springer.com/10.1007/s42990-020-00041-6 doi:10.1007/s42990-020-00041-6

Duman, T. Y., & Emre, Ö. (2013). The East Anatolian Fault: geometry, segmentation and jog characteristics. *Geol. Soc. London, Spec. Publ.*, *372*(1), 495–529. Retrieved from https://www.lyellcollection.org/doi/10.1144/SP372.14 doi:10.1144/SP372.14

Dunham, E. M., & Bhat, H. S. (2008). Attenuation of radiated ground motion and stresses from three-dimensional supershear ruptures. *J. Geophys. Res. Solid Earth*, *113*(B8), 1–17. Retrieved from http://doi.wiley.com/10.1029/2007JB005182 doi:10.1029/2007JB005182

Dziewonski, A. M., Chou, T.-A., & Woodhouse, J. H. (1981). Determination of earthquake source parameters from waveform data for studies of global and regional seismicity. *J. Geophys. Res. Solid Earth*, *86*(B4), 2825–2852. doi:10.1029/JB086iB04p02825

Ekström, G., Nettles, M., & Dziewoński, A. (2012). The global CMT project

2004–2010: Centroid-moment tensors for 13,017 earthquakes. *Phys. Earth Planet. Inter.*, *200-201*, 1–9. doi:10.1016/j.pepi.2012.04.002

Elson, P., de Andrade, E. S., Lucas, G., May, R., Hattersley, R., Campbell, E., … daryl herzmann (2022). *Scitools/cartopy: v0.21.1.* Zenodo. Retrieved from https://doi.org/10.5281/zenodo.7430317 doi:10.5281/zenodo.7430317

Emre, Ö., Duman, T. Y., Özalp, S., Şaroğlu, F., Olgun, , Elmacı, H., & Çan, T. (2018). Active fault database of Turkey. *Bull. Earthq. Eng.*, *16*(8), 3229–3275. doi:10.1007/s10518-016-0041-2

Fan, W., Okuwaki, R., Barbour, A. J., Huang, Y., Lin, G., & Cochran, E. S. (2022). Fast rupture of the 2009 M w 6.9 Canal de Ballenas earthquake in the Gulf of California dynamically triggers seismicity in California. *Geophys. J. Int.*, *230*(1), 528–541. Retrieved from https://doi.org/10.1093/gji/ggac059https://academic.oup.com/gji/article/230/1/528/6524846 doi:10.1093/gji/ggac059

Fan, W., & Shearer, P. M. (2015). Detailed rupture imaging of the 25 April 2015 Nepal earthquake using teleseismic P waves. *Geophys. Res. Lett.*, *42*(14), 5744–5752. doi:10.1002/2015GL064587

Fan, W., & Shearer, P. M. (2016). Local near instantaneously dynamically triggered aftershocks of large earthquakes. *Science*, *353*(6304), 1133–1136. doi:10.1126/science.aag0013

Fan, W., Shearer, P. M., Ji, C., & Bassett, D. (2016). Multiple branching rupture of the 2009 Tonga-Samoa earthquake. *J. Geophys. Res. Solid Earth*, *121*(8), 5809–5827. doi:10.1002/2016JB012945

Fang, J., Ou, Q., Wright, T. J., Okuwaki, R., Amey, R. M. J., Craig, T. J., … Maghsoudi, Y. (2022). Earthquake Cycle Deformation Associated With the 2021 M W 7.4 Maduo (Eastern Tibet) Earthquake: An Intrablock Rupture Event on a Slow-Slipping Fault From Sentinel-1 InSAR and Teleseismic Data. *J. Geophys. Res. Solid Earth*, *127*(11). Retrieved from https://onlinelibrary.wiley.com/doi/10.1029/2022JB024268 doi:10.1029/2022JB024268

Fliss, S., Bhat, H. S., Dmowska, R., & Rice, J. R. (2005). Fault branching and rupture directivity. *J. Geophys. Res. Solid Earth*, *110*(B6). Retrieved from https://doi.org/10.1029/2004JB003368 doi:https://doi.org/10.1029/2004JB003368

Hardebeck, J. L., & Shearer, P. M. (2002). A New Method for Determining First-Motion Focal Mechanisms. *Bull. Seismol. Soc. Am.*, *92*(6), 2264–2276. Retrieved from https://doi.org/10.1785/0120010200 doi:10.1785/0120010200

Hartzell, S. H., & Heaton, T. H. (1983). Inversion of strong ground motion and teleseismic waveform data for the fault rupture history of the 1979 Imperial Valley, California, earthquake. *Bull. Seismol. Soc. Am.*, *73*(6A), 1553–1583. doi:10.1785/BSSA07306A1553

Heimann, S., Kriegerowski, M., Isken, M., Cesca, S., Daout, S., Grigoli, F., … Vasyura-Bathke, H. (2017). *Pyrocko - An open-source seismology toolbox and library.* GFZ Data Services. doi:10.5880/GFZ.2.1.2017.001

Hicks, S. P., Okuwaki, R., Steinberg, A., Rychert, C. A., Harmon, N., Abercrombie, R. E., … Sudhaus, H. (2020). Back-propagating supershear rupture in the 2016 Mw 7.1 Romanche transform fault earthquake. *Nat. Geosci.*, *13*(9), 647–653. doi:10.1038/s41561-020-0619-9

Hicks, S. P., & Rietbrock, A. (2015). Seismic slip on an upper-plate normal fault during a large subduction megathrust rupture. *Nat. Geosci.*, *8*(12), 955–960. doi:10.1038/ngeo2585

Hu, Y., Yagi, Y., Okuwaki, R., & Shimizu, K. (2021). Back-propagating rupture evolution within a curved slab during the 2019 M w 8.0 Peru intraslab earthquake. *Geophys. J. Int.*, *227*(3), 1602–1611. Retrieved from https://academic.oup.com/gji/advance-article/doi/10.1093/gji/ggab303/6338111https://academic.oup.com/gji/article/227/3/1602/6338111 doi:10.1093/gji/ggab303

Huang, Y. (2018). Earthquake Rupture in Fault Zones With Along-Strike Material Heterogeneity. *J. Geophys. Res. Solid Earth*, *123*(11), 9884–9898. Retrieved from http://doi.wiley.com/10.1029/2018JB016354 doi:10.1029/2018JB016354

Hunter, J. D. (2007). Matplotlib: A 2D Graphics Environment. *Comput. Sci. Eng.*, *9*(3), 90–95. doi:10.1109/MCSE.2007.55

Ide, S., & Aochi, H. (2005). Earthquakes as multiscale dynamic ruptures with heterogeneous fracture surface energy. *J. Geophys. Res. Solid Earth*, *110*(B11), 1–10. Retrieved from http://doi.wiley.com/10.1029/2004JB003591 doi:10.1029/2004JB003591

Ishii, M., Shearer, P. M., Houston, H., & Vidale, J. E. (2005). Extent, duration and speed of the 2004 Sumatra-Andaman earthquake imaged by the Hi-Net array. *Nature*, *435*(7044), 933–936. doi:10.1038/nature03675

Jackson, J., & McKenzie, D. (1984). Active tectonics of the Alpine–Himalayan Belt between western Turkey and Pakistan. *Geophys. J. Int.*, *77*(1), 185–264. Retrieved from https://academic.oup.com/gji/article-lookup/doi/10.1111/j.1365-246X.1984.tb01931.x doi:10.1111/j.1365-246X.1984.tb01931.x

Jiang, Y., González, P. J., & Bürgmann, R. (2022). Subduction earthquakes controlled by incoming plate geometry: The 2020 M > 7.5 Shumagin, Alaska, earthquake doublet. *Earth Planet. Sci. Lett.*, *584*, 117447. Retrieved from https://linkinghub.elsevier.com/retrieve/pii/S0012821X22000838 doi:10.1016/j.epsl.2022.117447

Kame, N., Rice, J. R., & Dmowska, R. (2003). Effects of prestress state and rupture velocity on dynamic fault branching. *J. Geophys. Res. Solid Earth*, *108*(B5), 1–21. Retrieved from http://doi.wiley.com/10.1029/2002JB002189 doi:10.1029/2002JB002189

Kase, Y., & Day, S. M. (2006). Spontaneous rupture processes on a bending fault. *Geophys. Res. Lett.*, *33*(10), 1–4. Retrieved from http://doi.wiley.com/10.1029/2006GL025870 doi:10.1029/2006GL025870

Kikuchi, M., & Kanamori, H. (1991). Inversion of complex body waves-III. *Bull. Seism. Soc. Am.*, *81*(6), 2335–2350. doi:10.1785/BSSA0810062335

King, G. C., Stein, R. S., & Lin, J. (1994). Static stress changes and the triggering of earthquakes. *Bull. Seismol. Soc. Am.*, *84*(3), 935–953. doi:10.1785/BSSA0840030935

Laske, G., Masters, T. G., Ma, Z., & Pasyanos, M. (2013). Update on CRUST1.0 - A 1-degree Global Model of Earth's Crust. *Geophys. Res. Abstr. 15, Abstr. EGU2013-*

2658, *15*, Abstract EGU2013–2658. (https://igppweb.ucsd.edu/~gabi/crust1.html)

Lay, T., Duputel, Z., Ye, L., & Kanamori, H. (2013). The December 7, 2012 Japan Trench intraplate doublet (Mw 7.2, 7.1) and interactions between near-trench intraplate thrust and normal faulting. *Phys. Earth Planet. Inter.*, *220*, 73–78. Retrieved from https://linkinghub.elsevier.com/retrieve/pii/S0031920113000599 doi:10.1016/j.pepi.2013.04.009

Lay, T., & Kanamori, H. (1980). Earthquake doublets in the Solomon Islands. *Phys. Earth Planet. Inter.*, *21*(4), 283–304. Retrieved from https://linkinghub.elsevier.com/retrieve/pii/003192018090134X doi:10.1016/0031-9201(80)90134-X

Lin, J., & Stein, R. S. (2004). Stress triggering in thrust and subduction earthquakes and stress interaction between the southern San Andreas and nearby thrust and strike-slip faults. *J. Geophys. Res. Solid Earth*, *109*(B2), 1–19. doi:10.1029/2003jb002607

McKenzie, D. (1972). Active Tectonics of the Mediterranean Region. *Geophys. J. Int.*, *30*(2), 109–185. Retrieved from https://academic.oup.com/gji/article-lookup/doi/10.1111/j.1365-246X.1972.tb02351.x doi:10.1111/j.1365-246X.1972.tb02351.x

Melgar, D., Ganas, A., Taymaz, T., Valkaniotis, S., Crowell, B. W., Kapetanidis, V., … Öcalan, T. (2020). Rupture kinematics of 2020 January 24 Mw 6.7 Doğanyol-Sivrice, Turkey earthquake on the East Anatolian Fault Zone imaged by space geodesy. *Geophys. J. Int.*, *223*(2), 862–874. Retrieved from https://academic.oup.com/gji/article/223/2/862/5872486 doi:10.1093/gji/ggaa345

Melgar, D., Taymaz, T., Ganas, A., Crowell, B. W., Öcalan, T., Kahraman, M., & Tsironi, V. (2023). Sub- and super-shear ruptures during the 2023 Mw 7.8 and Mw 7.6 earthquake doublet in SE Türkiye. *EarthArXiv*. doi:10.31223/X52W9D

Meng, L., Ampuero, J. P., Stock, J., Duputel, Z., Luo, Y., & Tsai, V. C. (2012). Earthquake in a maze: Compressional rupture branching during the 2012 Mw 8.6 Sumatra earthquake. *Science*, *337*(6095), 724–726. doi:10.1126/science.1224030

Meng, L., Bao, H., Huang, H., Zhang, A., Bloore, A., & Liu, Z. (2018). Double pincer movement: Encircling rupture splitting during the 2015 Mw 8.3 Illapel earthquake. *Earth Planet. Sci. Lett.*, *495*, 164–173. Retrieved from https://doi.org/10.1016/j.epsl.2018.04.057 doi:10.1016/j.epsl.2018.04.057

Met Office. (2015). *Cartopy: a cartographic python library with a Matplotlib interface.* Retrieved from https://scitools.org.uk/cartopy doi:10.5281/zenodo.1182735

Nissen, E., Elliott, J. R., Sloan, R. A., Craig, T. J., Funning, G. J., Hutko, A., … Wright, T. J. (2016). Limitations of rupture forecasting exposed by instantaneously triggered earthquake doublet. *Nat. Geosci.*, *9*(4), 330–336. doi:10.1038/ngeo2653

Okubo, K., Rougier, E., Lei, Z., & Bhat, H. S. (2020). Modeling earthquakes with off-fault damage using the combined finite-discrete element method. *Comput. Part. Mech.*, *7*(5), 1057–1072. Retrieved from https://doi.org/10.1007/

s40571-020-00335-4https://link.springer.com/10.1007/s40571-020-00335-4 doi:10.1007/s40571-020-00335-4

Okuwaki, R., & Fan, W. (2022). Oblique Convergence Causes Both Thrust and Strike-Slip Ruptures During the 2021 M 7.2 Haiti Earthquake. *Geophys. Res. Lett.*, *49*(2), 1–12. Retrieved from https://onlinelibrary.wiley.com/doi/10.1029/2021GL096373 doi:10.1029/2021GL096373

Okuwaki, R., Hicks, S. P., Craig, T. J., Fan, W., Goes, S., Wright, T. J., & Yagi, Y. (2021). Illuminating a Contorted Slab With a Complex Intraslab Rupture Evolution During the 2021 Mw 7.3 East Cape, New Zealand Earthquake. *Geophys. Res. Lett.*, *48*(24), 1–13. Retrieved from https://onlinelibrary.wiley.com/doi/10.1029/2021GL095117 doi:10.1029/2021GL095117

Okuwaki, R., Hirano, S., Yagi, Y., & Shimizu, K. (2020). Inchworm-like source evolution through a geometrically complex fault fueled persistent supershear rupture during the 2018 Palu Indonesia earthquake. *Earth Planet. Sci. Lett.*, *547*, 116449. doi:10.1016/j.epsl.2020.116449

Okuwaki, R., Yagi, Y., Aránguiz, R., González, J., & González, G. (2016). Rupture Process During the 2015 Illapel, Chile Earthquake: Zigzag-Along-Dip Rupture Episodes. *Pure Appl. Geophys.*, *173*(4), 1011–1020. doi:10.1007/s00024-016-1271-6

Olson, A. H., & Apsel, R. J. (1982). Finite faults and inverse theory with applications to the 1979 Imperial Valley earthquake. *Bull. Seismol. Soc. Am.*, *72*(6A), 1969–2001. Retrieved from + doi:10.1785/BSSA07206A1969

Otsuki, K., & Dilov, T. (2005). Evolution of hierarchical self-similar geometry of experimental fault zones: Implications for seismic nucleation and earthquake size. *J. Geophys. Res. Solid Earth*, *110*(3), 1–9. doi:10.1029/2004JB003359

Perinçek, D., & Çemen, I. (1990). The structural relationship between the East Anatolian and Dead Sea fault zones in southeastern Turkey. *Tectonophysics*, *172*(3-4), 331–340. Retrieved from https://linkinghub.elsevier.com/retrieve/pii/004019519090039B doi:10.1016/0040-1951(90)90039-B

Pousse-Beltran, L., Nissen, E., Bergman, E. A., Cambaz, M. D., Gaudreau, É., Karasözen, E., & Tan, F. (2020). The 2020 M w 6.8 Elazığ (Turkey) Earthquake Reveals Rupture Behavior of the East Anatolian Fault. *Geophys. Res. Lett.*, *47*(13), 1–14. Retrieved from https://onlinelibrary.wiley.com/doi/10.1029/2020GL088136 doi:10.1029/2020GL088136

Ragon, T., Simons, M., Bletery, Q., Cavalié, O., & Fielding, E. (2021). A Stochastic View of the 2020 Elazığ M w 6.8 Earthquake (Turkey). *Geophys. Res. Lett.*, *48*(3), 1–13. Retrieved from https://onlinelibrary.wiley.com/doi/10.1029/2020GL090704 doi:10.1029/2020GL090704

Reitman, N. G., Briggs, R. W., Barnhart, W. D., Thompson Jobe, J. A., DuRoss, C. B., Hatem, A. E., … Mejstrik, J. D. (2023). Preliminary fault rupture mapping of the 2023 M7.8 and M7.5 Türkiye Earthquakes. doi:10.5066/P985I7U2

Ross, Z. E., Idini, B., Jia, Z., Stephenson, O. L., Zhong, M., Wang, X., … Jung, J. (2019). Hierarchical interlocked orthogonal faulting in the 2019 Ridgecrest earthquake sequence. *Science (80-.).*, *366*(6463), 346–351. Retrieved from https://www.science.org/doi/10.1126/science.aaz0109

doi:10.1126/science.aaz0109
Sato, D., Fukahata, Y., & Nozue, Y. (2022). Appropriate reduction of the posterior distribution in fully Bayesian inversions. *Geophys. J. Int.*, *231*(2), 950–981. doi:10.1093/gji/ggac231
Satriano, C., Kiraly, E., Bernard, P., & Vilotte, J.-P. (2012). The 2012 Mw 8.6 Sumatra earthquake: Evidence of westward sequential seismic ruptures associated to the reactivation of a N-S ocean fabric. *Geophys. Res. Lett.*, *39*(15). doi:10.1029/2012GL052387
Scholz, C. H., Ando, R., & Shaw, B. E. (2010). The mechanics of first order splay faulting: The strike-slip case. *J. Struct. Geol.*, *32*(1), 118–126. Retrieved from http://dx.doi.org/10.1016/j.jsg.2009.10.007https://linkinghub.elsevier.com/retrieve/pii/S0191814109002211 doi:10.1016/j.jsg.2009.10.007
Shimizu, K., Yagi, Y., Okuwaki, R., & Fukahata, Y. (2020). Development of an inversion method to extract information on fault geometry from teleseismic data. *Geophys. J. Int.*, *220*(2), 1055–1065. doi:10.1093/gji/ggz496
Socquet, A., Hollingsworth, J., Pathier, E., & Bouchon, M. (2019). Evidence of supershear during the 2018 magnitude 7.5 Palu earthquake from space geodesy. *Nat. Geosci.*, *12*(3), 192–199. Retrieved from http://dx.doi.org/10.1038/s41561-018-0296-0http://www.nature.com/articles/s41561-018-0296-0 doi:10.1038/s41561-018-0296-0
Tadapansawut, T., Okuwaki, R., Yagi, Y., & Yamashita, S. (2021). Rupture Process of the 2020 Caribbean Earthquake Along the Oriente Transform Fault, Involving Supershear Rupture and Geometric Complexity of Fault. *Geophys. Res. Lett.*, *48*(1), 1–9. doi:10.1029/2020GL090899
Taymaz, T., Eyidogan, H., & Jackson, J. (1991). Source parameters of large earthquakes in the East Anatolian Fault Zone (Turkey). *Geophys. J. Int.*, *106*(3), 537–550. Retrieved from https://academic.oup.com/gji/article-lookup/doi/10.1111/j.1365-246X.1991.tb06328.x doi:10.1111/j.1365-246X.1991.tb06328.x
Taymaz, T., Ganas, A., Yolsal-Çevikbilen, S., Vera, F., Eken, T., Erman, C., … Öcalan, T. (2021). Source Mechanism and Rupture Process of the 24 January 2020 Mw 6.7 Doğanyol–Sivrice Earthquake obtained from Seismological Waveform Analysis and Space Geodetic Observations on the East Anatolian Fault Zone (Turkey). *Tectonophysics*, *804*(January), 228745. Retrieved from https://linkinghub.elsevier.com/retrieve/pii/S0040195121000299 doi:10.1016/j.tecto.2021.228745
Taymaz, T., Jackson, J., & McKenzie, D. (1991). Active tectonics of the north and central Aegean Sea. *Geophys. J. Int.*, *106*(2), 433–490. Retrieved from https://academic.oup.com/gji/article-lookup/doi/10.1111/j.1365-246X.1991.tb03906.x doi:10.1111/j.1365-246X.1991.tb03906.x
Taymaz, T., Westaway, R., & Reilinger, R. (2004). Active faulting and crustal deformation in the Eastern Mediterranean region. *Tectonophysics*, *391*(1-4), 1–9. Retrieved from https://linkinghub.elsevier.com/retrieve/pii/S0040195104002173 doi:10.1016/j.tecto.2004.07.005
ten Brink, U., Wei, Y., Fan, W., Granja-Bruña, J.-L., & Miller, N. (2020). Mysterious tsunami in the Caribbean Sea following the 2010 Haiti earthquake possibly

generated by dynamically triggered early aftershocks. *Earth Planet. Sci. Lett.*, *540*, 116269. Retrieved from https://linkinghub.elsevier.com/retrieve/pii/S0012821X20302120 doi:10.1016/j.epsl.2020.116269

Toda, S., Stein, R. S., Richards-Dinger, K., & Bozkurt, S. B. (2005). Forecasting the evolution of seismicity in southern California: Animations built on earthquake stress transfer. *J. Geophys. Res. Solid Earth*, *110*(5), 1–17. doi:10.1029/2004JB003415

Trugman, D. T., & Dunham, E. M. (2014). A 2D Pseudodynamic Rupture Model Generator for Earthquakes on Geometrically Complex Faults. *Bull. Seismol. Soc. Am.*, *104*(1), 95–112. Retrieved from https://doi.org/10.1785/0120130138https://pubs.geoscienceworld.org/bssa/article/104/1/95-112/332165 doi:10.1785/0120130138

Tsai, V. C., & Hirth, G. (2020). Elastic Impact Consequences for High-Frequency Earthquake Ground Motion. *Geophys. Res. Lett.*, *47*(5), 1–8. Retrieved from https://onlinelibrary.wiley.com/doi/10.1029/2019GL086302 doi:10.1029/2019GL086302

Vallée, M., Xie, Y., Grandin, R., Villegas-Lanza, J. C., Nocquet, J. M., Vaca, S., … Rolandone, F. (2023). Self-reactivated rupture during the 2019 Mw=8 northern Peru intraslab earthquake. *Earth Planet. Sci. Lett.*, *601*, 117886. Retrieved from https://doi.org/10.1016/j.epsl.2022.117886 doi:10.1016/j.epsl.2022.117886

Wang, J., Xu, C., Freymueller, J. T., Wen, Y., & Xiao, Z. (2021). AutoCoulomb: An automated configurable program to calculate coulomb stress changes on receiver faults with any orientation and its application to the 2020 Mw7.8 Simeonof Island, Alaska, Earthquake. *Seismol. Res. Lett.*, *92*(4), 2591–2609. doi:10.1785/0220200283

Weiss, J. R., Walters, R. J., Morishita, Y., Wright, T. J., Lazecky, M., Wang, H., … Parsons, B. (2020). High-Resolution Surface Velocities and Strain for Anatolia From Sentinel-1 InSAR and GNSS Data. *Geophys. Res. Lett.*, *47*(17). Retrieved from https://onlinelibrary.wiley.com/doi/10.1029/2020GL087376 doi:10.1029/2020GL087376

Wessel, P., & Luis, J. F. (2017). The GMT/MATLAB Toolbox. *Geochemistry, Geophys. Geosystems*, *18*(2), 811–823. doi:10.1002/2016GC006723

Xu, S., Fukuyama, E., Ben-Zion, Y., & Ampuero, J.-P. (2015). Dynamic rupture activation of backthrust fault branching. *Tectonophysics*, *644-645*, 161–183. Retrieved from http://dx.doi.org/10.1016/j.tecto.2015.01.011https://linkinghub.elsevier.com/retrieve/pii/S0040195115000554 doi:10.1016/j.tecto.2015.01.011

Xu, Y., Koper, K. D., Sufri, O., Zhu, L., & Hutko, A. R. (2009). Rupture imaging of the Mw 7.9 12 May 2008 Wenchuan earthquake from back projection of teleseismic P waves. *Geochemistry, Geophys. Geosystems*, *10*(4), Q04006. doi:10.1029/2008GC002335

Yabuki, T., & Matsu'ura, M. (1992). Geodetic data inversion using a Bayesian information criterion for spatial distribution of fault slip. *Geophys. J. Int.*, *109*(2), 363–375. Retrieved from https://onlinelibrary.wiley.com/doi/abs/10.1111/j.1365-246X.1992.tb00102.xhttps://academic.oup.com/gji/

article-lookup/doi/10.1111/j.1365-246X.1992.tb00102.x doi:10.1111/j.1365-246X.1992.tb00102.x

Yagi, Y., & Fukahata, Y. (2011). Introduction of uncertainty of Green's function into waveform inversion for seismic source processes. *Geophys. J. Int.*, *186*(2), 711–720. doi:10.1111/j.1365-246X.2011.05043.x

Yagi, Y., Okuwaki, R., Enescu, B., & Lu, J. (2023). Irregular rupture process of the 2022 Taitung, Taiwan, earthquake sequence. *Sci. Rep.*, *13*(1), 1107. Retrieved from https://doi.org/10.1038/s41598-023-27384-yhttps://www.nature.com/articles/s41598-023-27384-y doi:10.1038/s41598-023-27384-y

Yamashita, S., Yagi, Y., & Okuwaki, R. (2022). Irregular rupture propagation and geometric fault complexities during the 2010 Mw 7.2 El Mayor-Cucapah earthquake. *Sci. Rep.*, *12*(1), 4575. Retrieved from https://doi.org/10.1038/s41598-022-08671-6https://www.nature.com/articles/s41598-022-08671-6 doi:10.1038/s41598-022-08671-6

Yamashita, S., Yagi, Y., Okuwaki, R., Shimizu, K., Agata, R., & Fukahata, Y. (2022). Potency density tensor inversion of complex body waveforms with time-adaptive smoothing constraint. *Geophys. J. Int.*, *231*(1), 91–107. Retrieved from https://academic.oup.com/gji/article/231/1/91/6584392 doi:10.1093/gji/ggac181

Yao, H., Gerstoft, P., Shearer, P. M., & Mecklenbräuker, C. (2011). Compressive sensing of the Tohoku-Oki Mw 9.0 earthquake: Frequency-dependent rupture modes. *Geophys. Res. Lett.*, *38*(20). doi:10.1029/2011GL049223

Yıkılmaz, M. B., Turcotte, D. L., Heien, E. M., Kellogg, L. H., & Rundle, J. B. (2015). Critical Jump Distance for Propagating Earthquake Ruptures Across Step-Overs. *Pure Appl. Geophys.*, *172*(8), 2195–2201. Retrieved from http://link.springer.com/10.1007/s00024-014-0786-y doi:10.1007/s00024-014-0786-y

Supporting Information for

Multi-scale rupture growth with alternating directions in a complex fault network during the 2023 south-eastern Türkiye and Syria earthquake doublet

Ryo Okuwaki[1], **Yuji Yagi**[1], **Tuncay Taymaz**[2], **Stephen P. Hicks**[3]

[1]Faculty of Life and Environmental Sciences, University of Tsukuba, Tsukuba, Ibaraki 305-8572, Japan
[2]Department of Geophysical Engineering, The Faculty of Mines, Istanbul Technical University, Maslak, 34469 Sariyer, Istanbul, Türkiye
[3]Department of Earth Sciences, University College London, Gower Street, London, WC1E 6BT, UK

Contents

Corresponding author: Ryo Okuwaki, `rokuwaki@geol.tsukuba.ac.jp`

Table S1. Near-source structure used for calculating Green's functions, adopted from CRUST1.0 model (Laske et al., 2013).

V_P (km/s)	V_S (km/s)	Density (g/cm^3)	Thickness (km)
6.00	3.52	2.72	17.64
6.30	3.68	2.79	8.90
6.60	3.82	2.85	9.64
8.08	4.49	3.33	- (below moho)

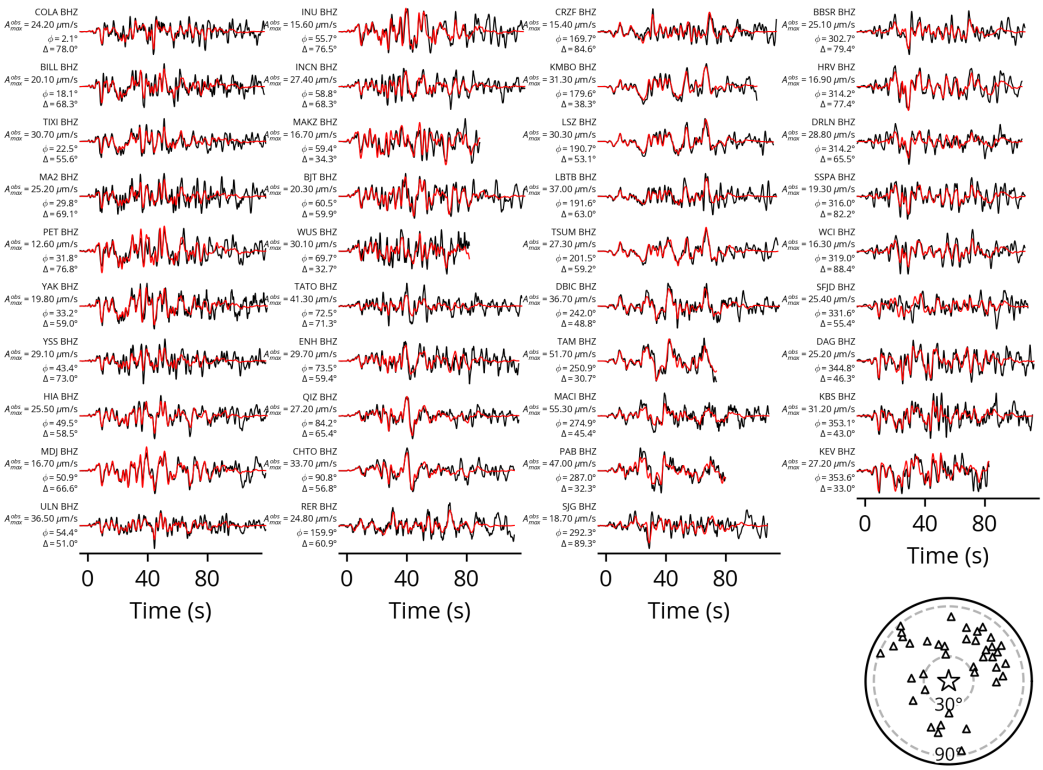

Figure S1. Waveform fits of the initial M_W 7.9 earthquake model. The black and red traces are the observed and synthetic waveforms. The station code and channel, the maximum amplitude of observed waveform (A^{obs}_{max}), the station azimuth (ϕ), and the epicentral distance (Δ) are shown on the left of each panel. The bottom map is an azimuthal equidistant projection of the station distribution (triangle). The star shows the epicenter. The dashed lines are the epicentral distances at 30° and 90°.

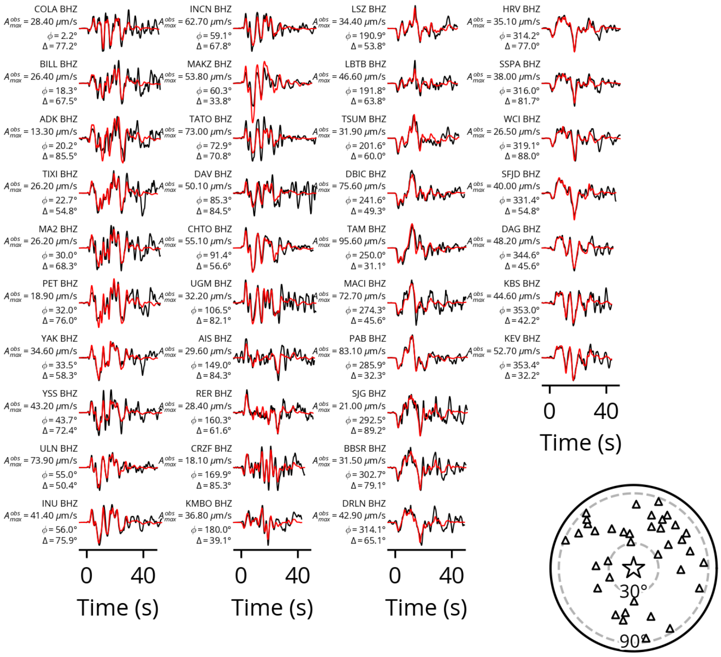

Figure S2. Waveform fits of the secondary M_W 7.6 earthquake model. The black and red traces are the observed and synthetic waveforms. The station code and channel, the maximum amplitude of observed waveform (A_{max}^{obs}), the station azimuth (ϕ), and the epicentral distance (Δ) are shown on the left of each panel. The bottom map is an azimuthal equidistant projection of the station distribution (triangle). The star shows the epicenter. The dashed lines are the epicentral distances at 30° and 90°.

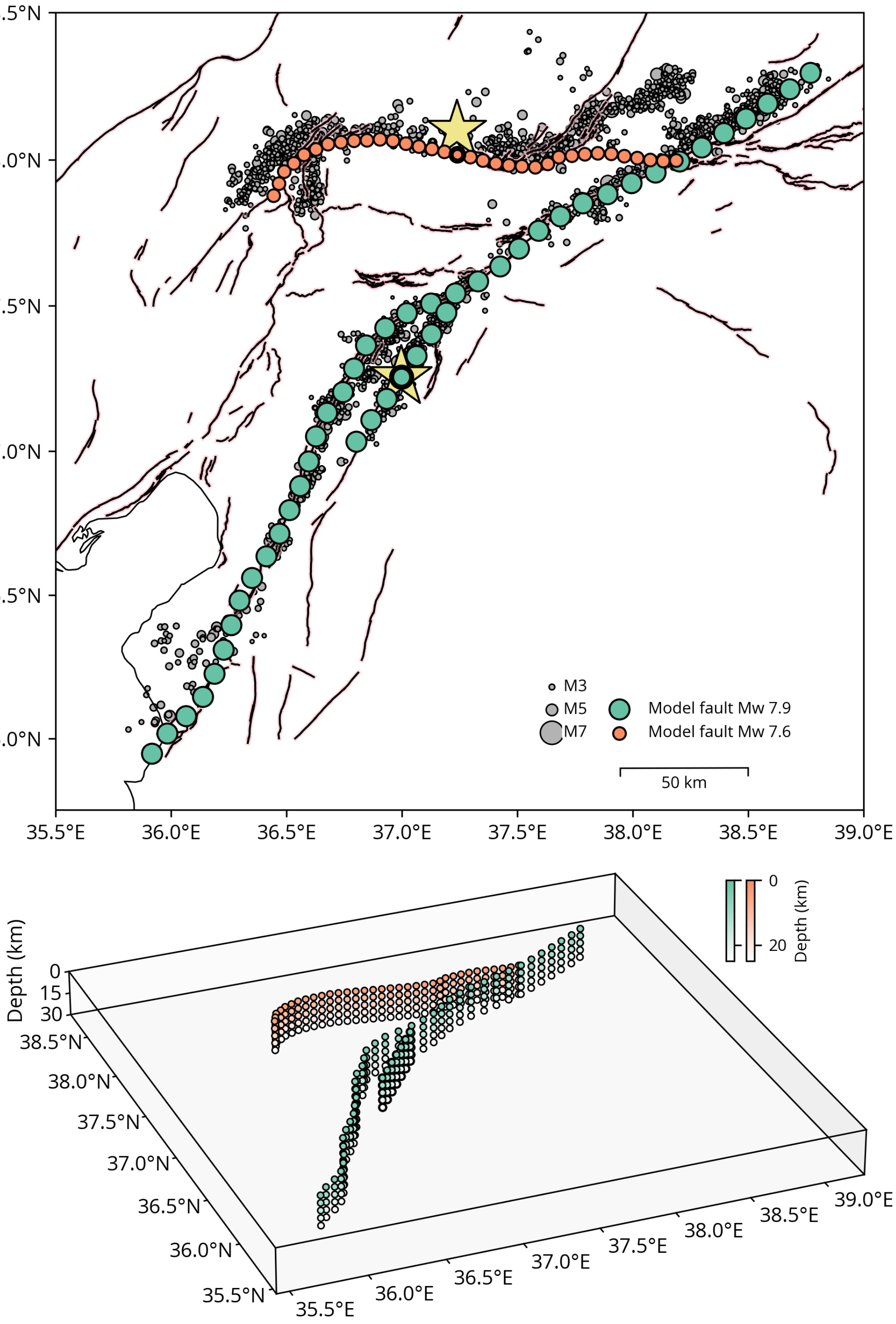

Figure S3. Model-fault geometries for the M_W 7.9 (green) and M_W 7.6 (orange) earthquakes used for our potency-density tensor inversion. The colored dots shows the location of the source elements. The hypothesized initial rupture point is marked as a thick black circle on a map. The relocated mainshocks (stars), aftershocks (gray dots), and active faults are the same as shown in Fig. 1.

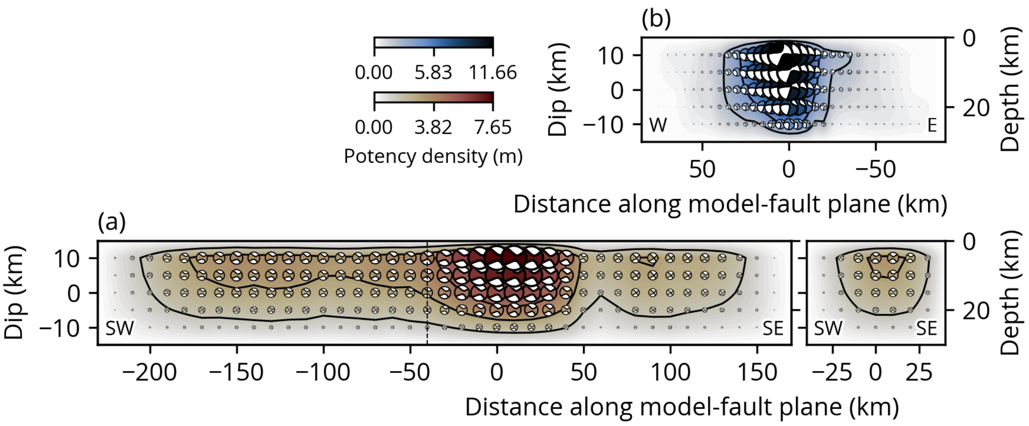

Figure S4. Cross sections of the total potency-density tensor distributions for (a) the M_W 7.9 (reddish) and (b) the M_W 7.6 (blueish) earthquakes. The beachball is the lower hemisphere projection of the moment tensor drawn by using Pyrocko (Heimann et al., 2017). The size of the beachball is scaled by potency density. The abscissa is a distance from the hypothesized initial rupture point along the non-planar model fault. For each panel, the vertical axis (Y-axis) is stretched by a factor of 2 for the visibility of the figure. The dashed line on panel (a) denotes the point on the EAF, which is closest to the initial rupture point on the splay model fault. The panel (b) is flipped horizontally so that it can intuitively be compared with map view of the corresponding model (M_W 7.6 earthquake) in Fig. 2. The black contours are drawn at every 1.5 m (lower panels) and 2.3 m (upper panel) for the M_W 7.9 and the M_W 7.6 earthquakes, respectively.

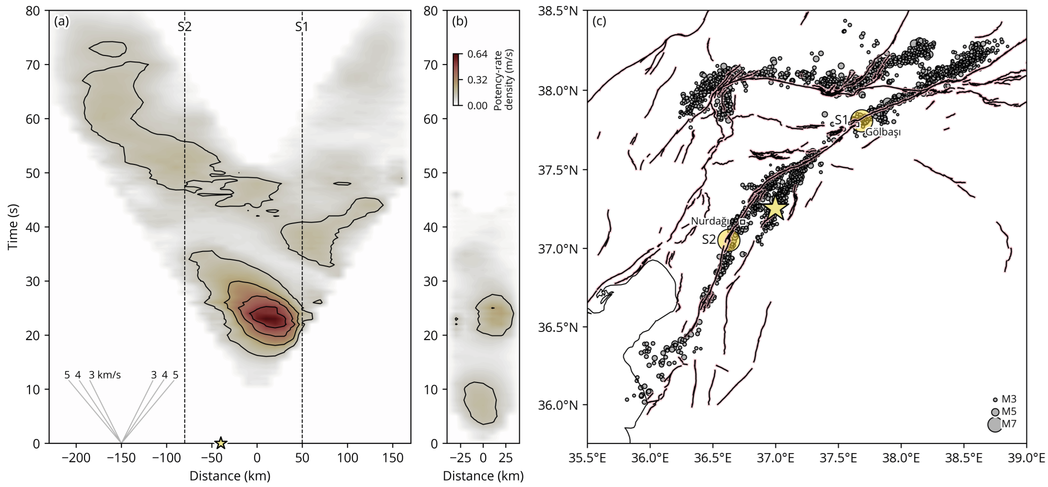

Figure S5. Comparison between (a) the potency-rate density tensor distribution and (b) the active faults. The dashed lines indicate the approximate positions of the steps, shown on a map (c) as S1 and S2. Panels (a,b) are from Fig. 2, and the active faults, the mainshocks, and the aftershocks are the same as shown in Fig. 1.

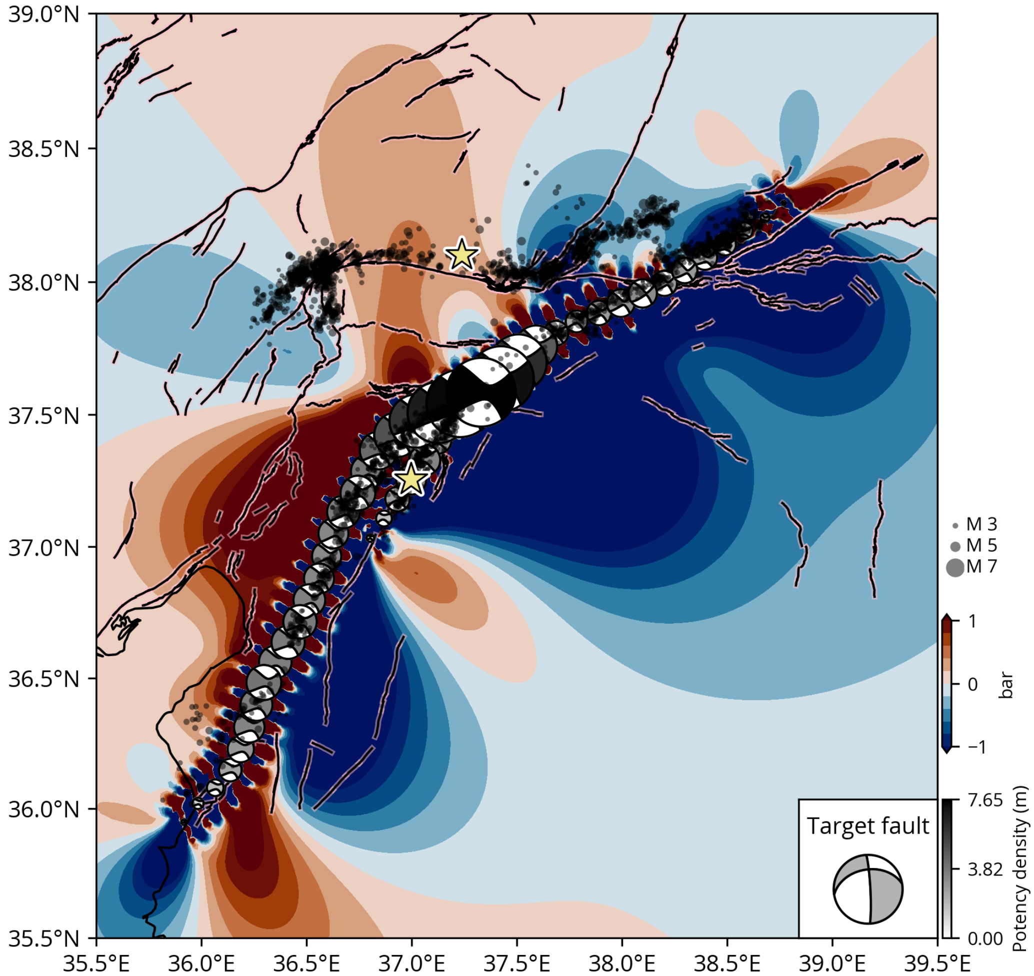

Figure S6. The Coulomb stress change (King et al., 1994; Lin & Stein, 2004; Toda et al., 2005; Wang et al., 2021) from our preferred solution (Fig. S4a) to the target fault of the M_W 7.6 earthquake (inset), averaged over 5–30 km depths. The Coulomb stresses are calculated with a friction coefficient of 0.4, poison ratio of 0.25, and Young's modulus of 8×10^5 bars. The target fault is of 261°/42°/−8° (strike/dip/rake) from the GCMT solution for the M_W 7.6 earthquake (Dziewonski et al., 1981; Ekström et al., 2012). The relocated mainshocks (stars), aftershocks (gray dots), and active faults are the same as shown in Fig. 1.

Movies S1 and S2 (caption)

Movie S1. Cross sections of the spatiotemporal potency-rate density tensor distribution for (a,b) the M_W 7.9 earthquake and (c) the M_W 7.6 earthquake. Panel (b) is the splay fault domain. The X-axis is the distance along the non-planar model-fault plane. The "0" on the X-axis means our hypothesized initial rupture point, except for Panel (a), which corresponds to the location of junction between the splay fault and the main EAF. The dashed line on Panel (a) denotes the point on the EAF, which is closest to the initial rupture point on the splay model fault. Note that Panel (c) is flipped horizontally so the right-hand side is orienting to east.

Movie S2. Map view of the spatiotemporal potency-rate density tensor distribution for the M_W 7.9 earthquake and M_W 7.6 earthquake. The size of the beachball is scaled by the maximum potency-rate density for each model. The moment-rate function (left top) and the temporal evolution of the potency-rate density distribution (right top) are the same as shown in Fig. 2. The epicenters (stars), aftershocks, and active faults are the same as shown in Fig. 1.

References in the Supporting Information

Dziewonski, A. M., Chou, T.-A., & Woodhouse, J. H. (1981). Determination of earthquake source parameters from waveform data for studies of global and regional seismicity. *J. Geophys. Res. Solid Earth*, *86*(B4), 2825–2852. doi:10.1029/JB086iB04p02825

Ekström, G., Nettles, M., & Dziewoński, A. (2012). The global CMT project 2004–2010: Centroid-moment tensors for 13,017 earthquakes. *Phys. Earth Planet. Inter.*, *200-201*, 1–9. doi:10.1016/j.pepi.2012.04.002

Heimann, S., Kriegerowski, M., Isken, M., Cesca, S., Daout, S., Grigoli, F., … Vasyura-Bathke, H. (2017). *Pyrocko - An open-source seismology toolbox and library.* GFZ Data Services. doi:10.5880/GFZ.2.1.2017.001

King, G. C., Stein, R. S., & Lin, J. (1994). Static stress changes and the triggering of earthquakes. *Bull. Seismol. Soc. Am.*, *84*(3), 935–953. doi:10.1785/BSSA0840030935

Laske, G., Masters, T. G., Ma, Z., & Pasyanos, M. (2013). Update on CRUST1.0 - A 1-degree Global Model of Earth's Crust. *Geophys. Res. Abstr. 15*, *Abstr. EGU2013-2658*, *15*, Abstract EGU2013–2658. (https://igppweb.ucsd.edu/~gabi/crust1.html)

Lin, J., & Stein, R. S. (2004). Stress triggering in thrust and subduction earthquakes and stress interaction between the southern San Andreas and nearby thrust and strike-slip faults. *J. Geophys. Res. Solid Earth*, *109*(B2), 1–19. doi:10.1029/2003jb002607

Toda, S., Stein, R. S., Richards-Dinger, K., & Bozkurt, S. B. (2005). Forecasting the evolution of seismicity in southern California: Animations built on earthquake stress transfer. *J. Geophys. Res. Solid Earth*, *110*(5), 1–17. doi:10.1029/2004JB003415

Wang, J., Xu, C., Freymueller, J. T., Wen, Y., & Xiao, Z. (2021). AutoCoulomb: An automated configurable program to calculate coulomb stress changes on receiver faults with any orientation and its application to the 2020 Mw7.8 Simeonof Island, Alaska, Earthquake. *Seismol. Res. Lett.*, *92*(4), 2591–2609. doi:10.1785/0220200283